The Galapagos Chip Platform for High-Throughput Screening of Cell Adhesive Chemical Micropatterns

Urandelger Tuvshindorj, Vanessa Trouillet, Aliaksei Vasilevich, Britta Koch, Steven Vermeulen, Aurélie Carlier, Morgan R. Alexander, Stefan Giselbrecht, Roman Truckenmüller, and Jan de Boer*

In vivo cells reside in a complex extracellular matrix (ECM) that presents spatially distributed biochemical and -physical cues at the nano- to micro-meter scales. Chemical micropatterning is successfully used to generate adhesive islands to control where and how cells attach and restore cues of the ECM in vitro. Although chemical micropatterning has become a powerful tool to study cell–material interactions, only a fraction of the possible micropattern designs was covered so far, leaving many other possible designs still unexplored. Here, a high-throughput screening platform called "Galapagos chip" is developed. It contains a library of 2176 distinct subcellular chemical patterns created using mathematical algorithms and a straightforward UV-induced two-step surface modification. This approach enables the immobilization of ligands in geometrically defined regions onto cell culture substrates. To validate the system, binary RGD/polyethylene glycol patterns are prepared on which human mesenchymal stem cells are cultured, and the authors observe how different patterns affect cell and organelle morphology. As proof of concept, the cells are stained for the mechanosensitive YAP protein, and, using a machine-learning algorithm, it is demonstrated that cell shape and YAP nuclear translocation correlate. It is concluded that the Galapagos chip is a versatile platform to screen geometrical aspects of cell–ECM interaction.

1. Introduction

Cells sense and respond to the local environment through cell adhesions,[1,2] which also play a significant role in regulating fundamental cell functions, such as migration,[3–5]

differentiation,[6–10] and even survival.[11,12] Thus, understanding and controlling cell adhesion is essential for developing regenerative medicine and tissue engineering techniques, to advance in vitro cell assays and new biomaterial designs.

Early cell-material studies are mainly based on controlling cell adhesion through surface chemistry and mimicking the biochemical composition of the extracellular matrix (ECM) by uniformly modifying the material surface with biomolecules and cell adhesion ligands.[13–15] Various surface modification techniques are known, such as self-assembled monolayers,[16–19] polymer brushes,[20–22] and surface adsorption,[17,23] which enable a precisely controlled surface chemistry and the presentation of bioactive ligands. Beyond the biochemical composition, ECM also contains geometric cues: ECM proteins organize in fibrils and adhesive sites are dispersed over the proteins creating a geometrical landscape of ligands available for receptor-mediated adhesion.[1,24]

The development of micro and nanofabrication technologies and photochemistry[25–31] started to reveal how these complex geometric and biochemical interactions work, how cells perceive mechanical/chemical cues, and how signal transduction is activated.[7,32–34] For example, nanoscale patterning methods helped to understand that ligand density and integrin clustering control

---

U. Tuvshindorj, S. Vermeulen, A. Carlier, S. Giselbrecht, R. Truckenmüller
MERLN Institute for Technology-Inspired Regenerative Medicine
Maastricht University
Maastricht 6229 ER, The Netherlands

U. Tuvshindorj, A. Vasilevich, J. de Boer
Department of Biomedical Engineering and Institute for Complex Molecular Systems
Eindhoven University of Technology
Eindhoven 5600 MB, The Netherlands
E-mail: j.d.boer@tue.nl

V. Trouillet
Institute for Applied Materials and Karlsruhe Nano Micro Facility
Karlsruhe Institute of Technology
76344 Eggenstein-Leopoldshafen, Germany

B. Koch, M. R. Alexander
Advanced Materials and Healthcare Technologies Division
The School of Pharmacy
University of Nottingham
Nottingham NG7 2RD, UK

**ADVANCED
SCIENCE NEWS**

www.advancedsciencenews.com

**NANO · MICRO
small**

www.small-journal.com

focal adhesion (FA) size and maturation.[24,35–38] On the other hand, micropatterning methods at cell length-scale allowed the confinement of single cells in certain shapes and are used as a strategy to reveal the relation between cell shape and cell function.[8–11,39–41] For example, Chen et al. showed that apoptosis of endothelial cells can be controlled by altering the size of the ECM protein pattern that the cells can attach to[11] and how Rho-mediated signaling in mesenchymal stem cells (MSCs) controls differentiation toward adipogenesis and osteogenesis.[8] In addition, not only the size, but also the shape of the pattern of the ECM protein affects adipogenic and osteogenic differentiation.[9] However, little is known regarding the effects of subcellular pattern dimensions in the 1–20 µm range on cell function.[42]

Because engineering methods allow precise, subcellular control of adhesive pattern geometry, the design space of potential adhesive geometrical patterns is virtually unlimited and still largely unexplored. High-throughput platforms[43–46] offer the possibility to explore large design spaces as they have done for materials properties, such as material chemistry,[47–49] surface chemistry,[25,50] and surface topography.[51–54] We developed the TopoChip platform to study topography–cell interaction in high throughput. The platform was designed using a random pattern generator and produced using microfabrication techniques resulting in a library of 2176 unique topographies in the micrometer range.[51] We discovered many bio-active surfaces, which can control cell behavior based on a number of screens,[55–58] such as enhancing-induced pluripotent stem cells (iPSC) culture,[56] macrophage attachment and polarization,[57] and tenocyte phenotype maintenance.[58]

In this work, we present the Galapagos chip to expand high-throughput screening systems with subcellular chemical patterns, which allows the investigation of a library of subcellular range biochemical ligands and their interaction with cells. The Galapagos chip consists of the 2176 TopoChip patterns,[51] but now created as subcellular covalently bound dual-ligand patterns. Systematic investigation of cell response requires large substrate areas and a reproducible uniform grafting strategy. Accordingly, we optimized an alkene tail organosilane-based surface modification protocol to graft thiol-containing ligands via deep UV light and a photomask in a spatial controlled way. To show the functionality of the Galapagos chip, we measured nuclear translocation of the mechanosensitive transcription factor Yes-associated protein (YAP) in single cells. YAP is one of the main players in regulating cellular mechanotransduction and cell shape. The response to the mechanical stimulation and cell shape changes, YAP translocates between the cytoplasm and the nucleus, and regulates gene expression.[59,60] Measuring YAP helped to understand cell morphological and mechanotransduction effects of the subcellular micropatterns.

2. Results and Discussion

2.1. Surface Functionalization Strategy and Characterization

To functionalize biomaterial surfaces with different geometric patterns, we utilized single-step vapor-phase organosilane surface modification followed by photoinitiated thiol–ene click chemistry. In this combined approach, silane surface functionalization provides versatility because it allows the modification of different types of substrates such as polymers,[14] silicon,[18] and metals,[61] and the thiol–ene reaction yields selective coupling of bioligands in mild conditions, which prevents loss of bioactivity of the ligands.[62,63]

The general surface modification method and chemical routes are shown in **Figure 1**A. To create a thiol-reactive monolayer of alkene groups, we tested two different organosilanes with the most reactive alkene tails: norbornene-triethoxysilane (NbTES) and vinyltrimethoxysilane (VTMS).[63] A critical parameter of this chemical micropatterning protocol is the organosilane layer quality. The -trimethoxy, -triethoxy silane surface modifications tend to multimerize on the surfaces and increase the surface roughness uncontrollably.[61,64] This problem has been reduced previously by vapor-phase modification with a definite reaction time.[65] Therefore, the organosilanes were vapor-deposited onto the activated substrate. To optimize silanization time, the vapor deposition kinetics were monitored by measuring the static water contact angle (WCA) of VTMS-modified surfaces on a glass substrate. In the first 15 min, WCA increased rapidly from 8° to 54°, reaching a plateau of 77° after 24 h (Figure S1, Supporting Information). Accordingly, the silanization time was set to 24 h. The resulting silane-modified surface topography was characterized by tapping mode atomic force microscopy (AFM) measurements before and after surface modification (Figure 1B). The surface roughness increased slightly after modification with NbTES as indicated in the root mean square value of 1.1 ± 0.2 nm compared to 0.8 ± 0.1 nm of the activated glass substrate. For the VTMS treatment, a greater increase in surface roughness to 2.5 ± 0.1 nm was observed compared to the base activated glass surface. This greater increase suggests that VTMS formed a multilayer rather than a monolayer on the surface.[66] Despite that, for VTMS grafting, the surface appears homogenous, and no visible formation of aggregates or particles was observed above the nanometer scale (≈10 nm in height and ≈50 nm across) texture.

Next, we examined UV-activated thiol–ene coupling to the silane layers. Some of the thiol structures used in the study are shown in Figure 1C. For coupling, the alkene surface was wetted with a thiol solution of interest, covered with a quartz slide, and irradiated with 254 nm UV light (10 mW cm^{-2}). To optimize the thiol–ene reaction, we monitored the WCA of the surfaces after exposure to UV light for different irradiation times. The WCA of the VTMS-modified surface increased with 1H,1H,2H,2H-perfluorodecanethiol grafting from 76° to 101°, and decreased with RGD peptide grafting from 76° to 49° after 5 min of UV irradiation (Figure 1D). The WCA remained the same for longer irradiation times in both cases. For the NbTES-modified surface, static WCA decreased from 74° to 48° after RGD peptide grafting for 1 min under UV and remained stable afterward, demonstrating fast reaction kinetics.

Surface modification steps were confirmed by X-ray photoelectron spectroscopy (XPS) analysis. The data are shown in Figure 1E and Table S1 and Figure S2 in the Supporting Information. Since both silanes are composed only of silicon, oxygen, and carbon, no significant difference can be observed between the spectra of the glass substrate before and after silane modification. Therefore, we compared the N 1s core-level spectra from RGD-grafted
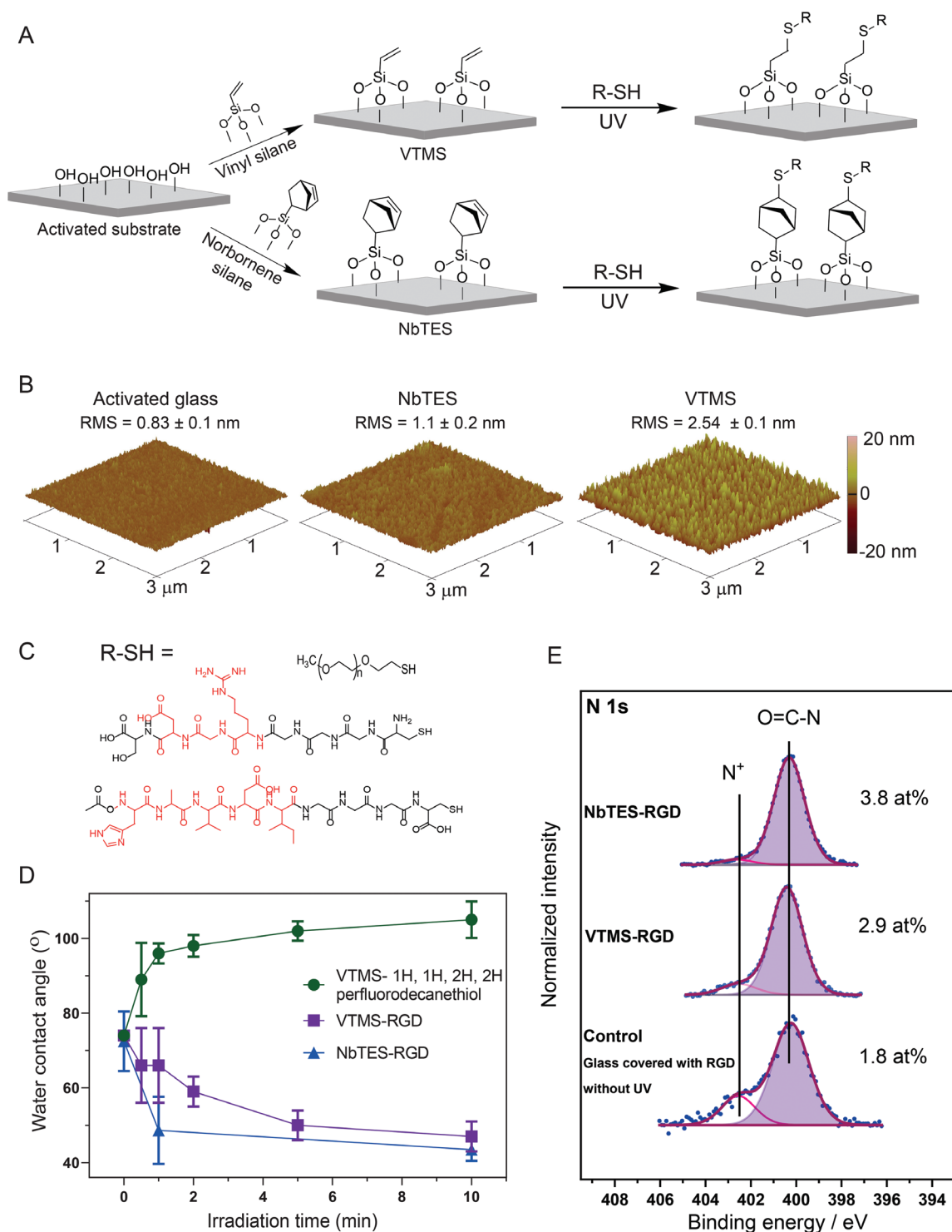
Figure 1. Surface functionalization strategy and characterization A) Schematic representation of the surface modification strategy. The method involves a piranha-treated-/-activated glass surface, which reacts with vinyl (VTMS) or norbornene silane (NbTES) to form reactive alkenes on the substrate and subsequent functionalization with a thiol of interest with UV-induced thiol–ene click chemistry. B) AFM image of an activated glass substrate before and after NbTES and VTMS modification. C) Thiols used: different molecular weight PEG-thiols, CGGGRGDS (RGD), and AcHAVDIGGGC (HAVDI) peptides, from top to bottom. D) Reaction kinetics of the thiol–ene photoreaction. The water contact angle of glass substrates modified with *1H,1H,2H,2H*-perfluorodecanethiol-grafted (green circle), and RGD peptide-grafted VTMS (purple square), and RGD peptide-grafted NbTES (blue triangle) as a function of UV (254 nm) irradiation time. Error bars represent standard deviation, $n = 3$ (number of independent samples). E) Comparison of the high-resolution XPS scans of the N 1s region for the RGD-grafted VTMS (VTMS-RGD), RGD-grafted NbTES (NbTES-RGD), and the control surface (glass surface treated with RGD without UV). Raw data are given in blue circles, while the sum of the fitted peaks is shown as a red line.

ADVANCED
SCIENCE NEWS
www.advancedsciencenews.com

NANO · MICRO
small
www.small-journal.com

VTMS and NbTES surfaces with a nonmodified glass surface incubated with RGD as a negative control to verify the reactivity of the surface containing alkenes (Figure 1E). Before grafting, less than 0.5 at% nitrogen could be detected at the glass surface indicating some nitrogen contamination (data not shown). After grafting, the alkene surfaces with RGD exhibited two distinct peaks at 400.0 and 402.6 eV, corresponding to amide N−C=O and protonated amine environments N^+, respectively, indicating successful surface functionalization with the RGD peptide. The nitrogen content increased to 3.8 and 2.9 at% for NbTES-RGD and VTMS-RGD surfaces, respectively. In the control measurement, we used nonmodified glass surfaces incubated in RGD peptide solution. Some nitrogen in peptide and protonated form could be detected also here. However, the nitrogen content was much lower than in the case of RGD-grafted alkene surfaces, indicating admittedly still some surface chemisorption of RGD on the glass surface but proving the efficiency of thiol–ene coupling. Similarly, in Figure S2 in the Supporting Information, we show the analysis of the high-resolution spectra of C 1s of VTMS and NbTES surfaces grafted with polyethylene glycol (PEG) thiol and of the nonmodified glass surface incubated with PEG as a negative control. The C 1s signal can be deconvoluted into three components at 288.8, 286.8, and 285.0 eV, assigned to O=C−O/O=C−N, C−O/C−N, and C−C/C−H carbon environments, respectively. VTMS-PEG and NbTES-PEG surfaces show a higher C−O contribution compared to VTMS, NbTES, and control surfaces, which indicates a successful surface reaction with the PEG–thiol. The efficiency of the reaction is clearly higher for VTMS in comparison to NbTES, especially for PEG–thiol coupling. In addition, from the XPS quantitative analysis (Table S1, Supporting Information), thiol–ene-coupled surfaces such as VTMS-RGD, VTMS-HAVDI, VTMS-PEG(2k), and NbTES-RGD all contain sulfur (S) which indicates thiol–ene coupling except for NbTES-PEG. A possible explanation for the absence of S 2p signal with S $2p_{3/2}$ at 163.4 eV in NbTES-PEG is that the coupling efficiency is too low so that the sulfur concentration is below the detection limit. These XPS results confirm that thiols can be covalently attached to the alkene-tailed silane-modified surfaces via UV-induced click reactions.

When comparing VTMS and NbTES coupling strategies from the XPS analysis (Table S1, Supporting Information), norbornene has the fastest reaction kinetics and a lower grafting efficiency, especially for PEG-modified surfaces. This could be a result of the lower level of silane functionalization achieved with NbTES compared to VTMS, due to the size and the chemical nature of the molecule.[30] Thus, in the rest of the study, we used a VTMS-based surface grafting strategy.

2.2. Bioactivity of Modified Surfaces

Next, we investigated whether our method is sufficient to graft different thiols as well as if the grafted peptides and thiols maintain bioactivity after the surface modification. Human mesenchymal stem cells (hMSCs) were seeded onto VTMS-functionalized glass, which was grafted with different thiols uniformly, so without patterns. The following thiol ligands were used: linear PEGs with molecular weights of 800 Da, 2 kDa, and 5 kDa, a 4-arm PEG with a molecular weight of 5 kDa, and cystine-terminated RGD and HAVDI peptides

(Figure 1C). RGD is a tripeptide motif present in many ECM proteins as integrin ligand,[67] and HAVDI is an N-cadherin binding motif.[68] We observed that different PEGs and different peptides modulated adhesion and spreading of hMSCs (**Figure 2**). We found that the antifouling property of PEG is molecular weight-dependent, which is in line with the literature:[69] 800 Da PEG-grafted surfaces failed to prevent cell adhesion whereas 4-arm 5 kDa, linear 2 kDa, and 5 kDa PEG modifications exhibited excellent antifouling properties. Also, we observed that a thick layer of PEG was formed after grafting of the 4-arm PEG–thiol, which indicates polymerization during UV irradiation through S−S bonding. We further observed that the grafted RGD and HAVDI peptides both promote hMSC adhesion on the glass substrate and thus maintain their bioactivity after grafting,[68] which is comparable to tissue culture polystyrene (TCP), but significantly lower than fibronectin-coated glass surfaces. In addition, cell area was comparable between fibronectin, TCP, RGD, and HAVDI. No significant difference was observed between integrin (RGD) and cadherin (HAVDI) adhesive ligand-modified surfaces in terms of the number of cells adhered to the surface and the cell area.

2.3. Fabrication of the Galapagos Chip

To fabricate a high-throughput platform with subcellular binary patterns, we used a quartz-chromium photomask with a design in the form of a previously reported library of 2176 distinct micropatterned units created using a mathematical design algorithm (**Figure 3**A).[51] The mask design was transferred using thiol–ene photoreaction to the substrate to form chemical micropatterns. First, the VTMS-modified surface was covered by the first thiol solution followed by UV irradiation through a photomask for 5 min. Finally, the whole surface was covered with a second thiol solution and irradiated again for 5 min through a blank quartz slide. This modification resulted in two different thiol ligands grafted in a spatially controlled way (Figure 3B). The example of the binary micropatterned glass surface grafted with fluorescein-labeled PEG, and rhodamine-labeled RGD peptide, is shown in Figure 3C. The micropatterns were characterized by time-of-flight secondary ion mass spectrometry (ToF-SIMS) (inset of Figure 3C), showing a clear pattern of the sum of CN^- and CNO^- ions, which demonstrates the patterning of the RGD peptide and a good contrast between the irradiated and nonirradiated areas. The spatial resolution is limited by the thickness of the thiol solution in the gap between the substrate and the mask. By decreasing the thiol solution volume, we decreased the substrate-mask proximity for optimal resolution (Figure S3, Supporting Information). Our optimized protocol is well-suited for generating dual ligand/peptide patterns via thiol–ene reaction on the glass substrate; however, it is essential to optimize UV coupling conditions to produce high-quality patterns when using different materials. To show the presented protocol is compatible with materials other than glass, we functionalized surfaces of polycarbonate (PC) and polyethylene (PE, coverslip from *ibidi*) with the silanes and patterned PE surface with fluorescein-labeled PEG (Figure S4, Supporting Information).
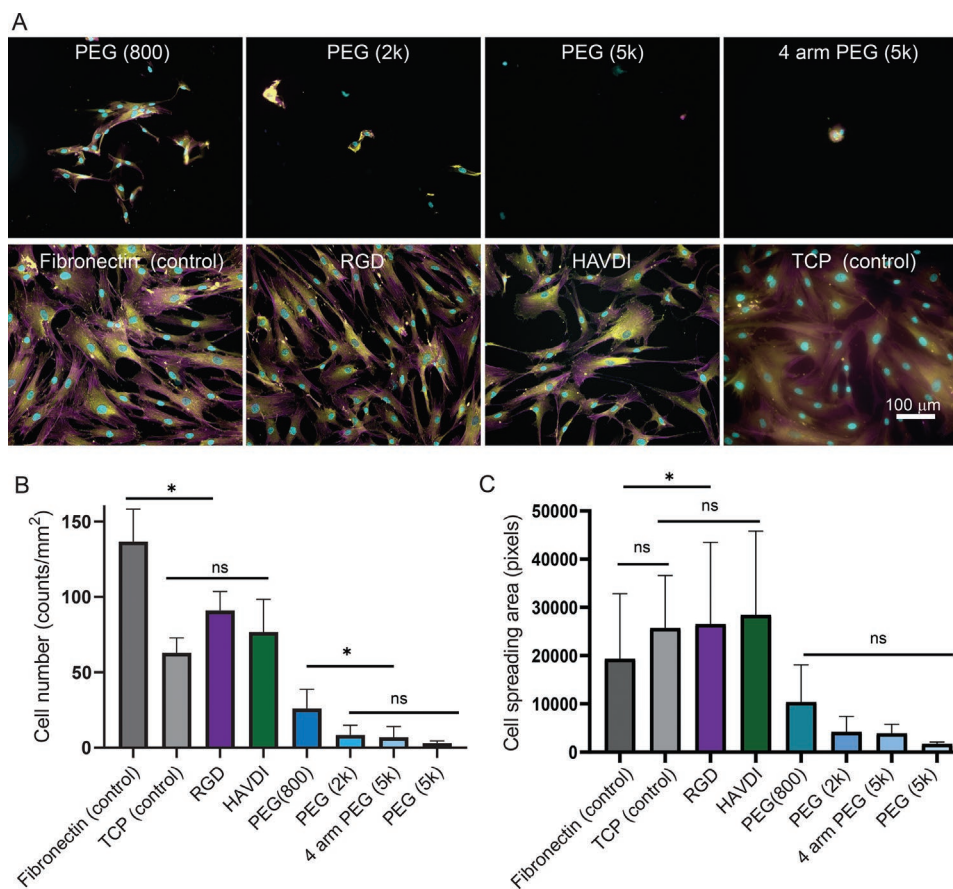
Figure 2. Cell adhesion and spreading on different thiol ligands. A) Human mesenchymal stem cells (hMSCs) adhering after 24 h on different thiol-grafted surfaces. Top row (left to right): PEGs with different molecular weights, PEG (800), PEG (2k), PEG (5k), and 4-arm PEG (5k). Bottom row (left to right): Fibronectin-coated glass substrate, HAVDI, and RGD-modified surfaces and tissue culture plate (TCP) as a control. Cells are stained for vinculin (yellow), nuclei (blue), and F-actin (purple). Scale bar is 100 µm. B) Total number of adhered hMSCs after 24 h per surface area on different thiol-functionalized surfaces. C) hMSC area per cell. Error bars represent SD, $n = 3$ (number of technical replicates) and significant difference expressed as * ($p < 0.05$).

2.4. hMSC Morphology and Subcellular Features Are Altered by the Underlying RGD Micropatterns

As proof of concept for high-throughput screening, we chose to graft the RGD peptide and the 2 kDa-PEG–thiol sequentially to fabricate the Galapagos chip, a name inspired by the geometrical and biological diversity in the namesake Ecuadorian archipelago. Based on our cell adhesion data, the 2 kDa-PEG–thiol was selected for patterning together with the RGD to maintain robust antifouling to study the specificity of the peptide and the corresponding micropatterns.[30] hMSCs were seeded onto the Galapagos chip and stained with the CellPainting assay[70] for visualizing cell morphology after 4 h. Visual inspection of the chip confirmed that different cellular morphologies were induced by different RGD microislands (**Figure** 4A and Figure S5, Supporting Information). Unlike single cell size micropatterns, which are used for restricting single cell shape,[34] on the Galapagos chip, cells can reside on multiple islands due to the low inter-pattern distance (<30 µm).[71] As shown in Figure 4A, the cells only attached and extended along the RGD patterns, avoiding the antifouling PEG polymer region. Cells on smaller microislands show smaller protrusions compared to the cells

on the bigger micropatterns and thus induce different cell morphologies. Besides the evident changes in cell morphologies, we observed differences in subcellular traits with the Cell-Painting assay, which stains seven subcellular structures: DNA, endoplasmic reticulum, Golgi, F-actin, the plasma membrane, nucleoli, and mitochondria. For example, in Figure 4B, cells on pattern Y (small pattern with big inter-pattern distance) have a brighter ER compared to the cells on pattern X (big pattern with small inter-pattern distance). The clear difference in cell morphology is already apparent 4 h after seeding. Also, we checked cell viability in the Galapagos chip to test the biocompatibility of the platform (Figure S6, Supporting Information). We did not see any differences regarding cell viability in 4 and 24 h culture of hMSCs on the platform compared to the tissue culture plate (TCP)."

2.5. High-Throughput Screening of Nuclear Localization of YAP

Adhesive islands induce a very diverse array of cell shapes, so we investigated how micropatterns can control mechanotransduction by staining three of its molecular players:[59,60,72,73]
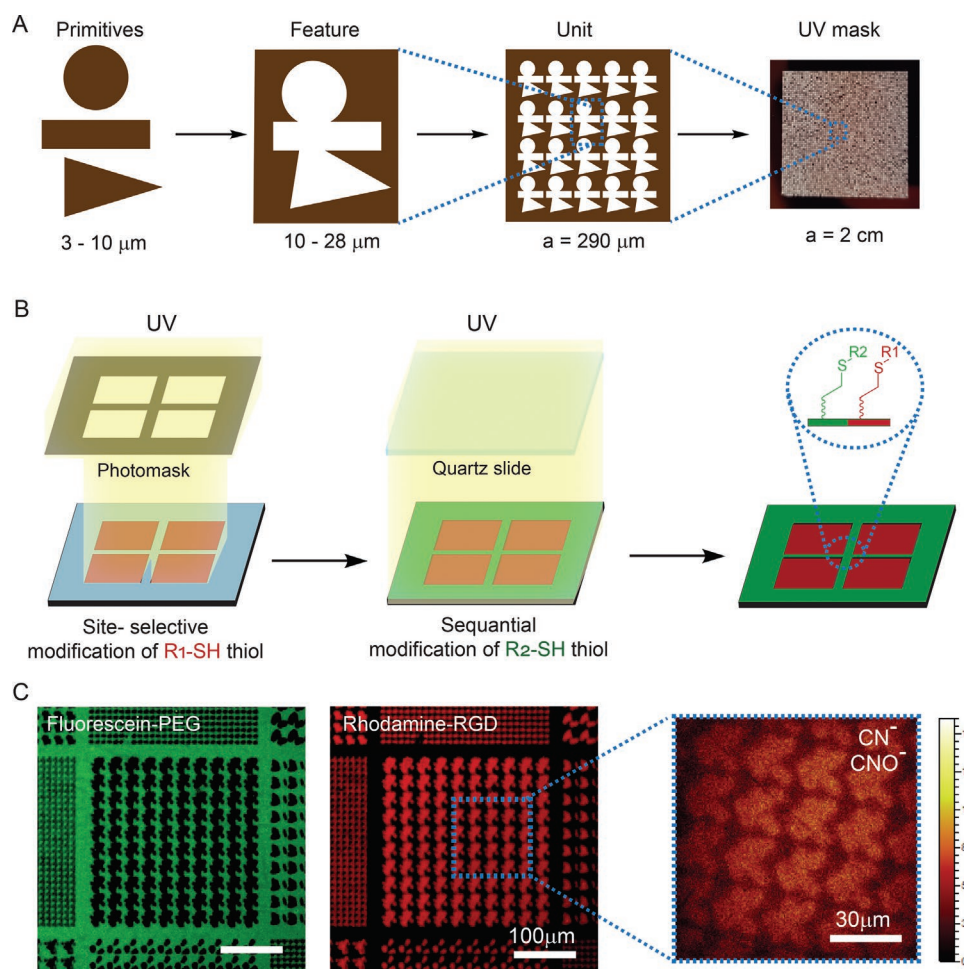
Figure 3. Development of the binary-functionalized Galapagos chip platform. A) Design of the platform. The primitive circles, triangles, and rectangles are randomly arranged into specific features that are multiplied and arrayed in a 290 μm × 290 μm area to form a single micropattern unit. 2176 unique units are duplicated in a 2 cm × 2 cm area to form the platform. The platform design is used to make the quartz mask. B) Schematic representation of the UV-induced thiol–ene reaction for creating binary micropatterns on vinyl-silane-functionalized glass substrate. Two different thiols (R1-SH and R2-SH) were sequentially grafted to the substrate using the photomask. C) Fluorescence microscope image of a part of the Galapagos chip functionalized with fluorescein-labeled PEG and rhodamine-labeled RGD peptide. Scale bar is 100 μm. In the inset image, ToF-SIMS 2D image of the sum of CN^- and CNO^- ions, showing the surface distribution of the RGD peptide. Scale bar is 30 μm.

paxillin which stains FAs, F-actin, and the mechanosensitive YAP. We seeded hMSCs onto six Galapagos chips and six uniformly coated RGD control surfaces. After 4 h, hMSCs were fixed and stained, as mentioned above. We noticed very diverse profiles of paxillin, F-actin, and YAP (**Figure 5**A) on Galapagos chip patterns compared to cells on uniformly grafted RGD surfaces (Figure 5B). On the uniformly grafted RGD surfaces, paxillin-stained FAs were not restricted and relatively long (up to 20 μm long) and extensive actin stress fibers were observed (see Figure 5B), which indicates mature FAs and high cytoskeletal tension in the cells. However, on Galapagos chip islands, FA formation was restricted to the underlying RGD pattern, and FA length depended on pattern dimension. FAs appeared most prominent on the edge of the RGD patterns when located on cell borders, regardless of the pattern size. Also, we noted that most cells on the pattern had actin stress fibers, and on the merged image, actin stress fiber ends colocalized with the FA edges.[74] We observed less

intense, more peripheral FAs and more cortical actin in the hMSCs cultured on small patterns with high inter-pattern distance (see last 2 rows of Figure 5A), which implies that these had less cytoskeleton tension. Our observations are in line with the current literature that subcellular adhesive micropatterns govern FA and cytoskeletal organization of cells.[1,71,74]

As seen in Figure 5A, YAP was located mostly in the cell nucleus on the Galapagos chip. Only for the cells on relatively small patterns with high inter-pattern distance, YAP was predominantly cytoplasmic, which correlated to less intense focal adhesion and less actin stress fibers. To quantify the range of YAP nuclear localization on all 2176 Galapagos chips units, we determined the mean YAP nuclear-to-cytoplasmic ratio of cells for each micropattern unit (Figure 5C, see Figure S7 in the Supporting Information for quantification of YAP expression level). hMSCs on the uniform RGD surfaces served as a reference, as indicated by the green line,
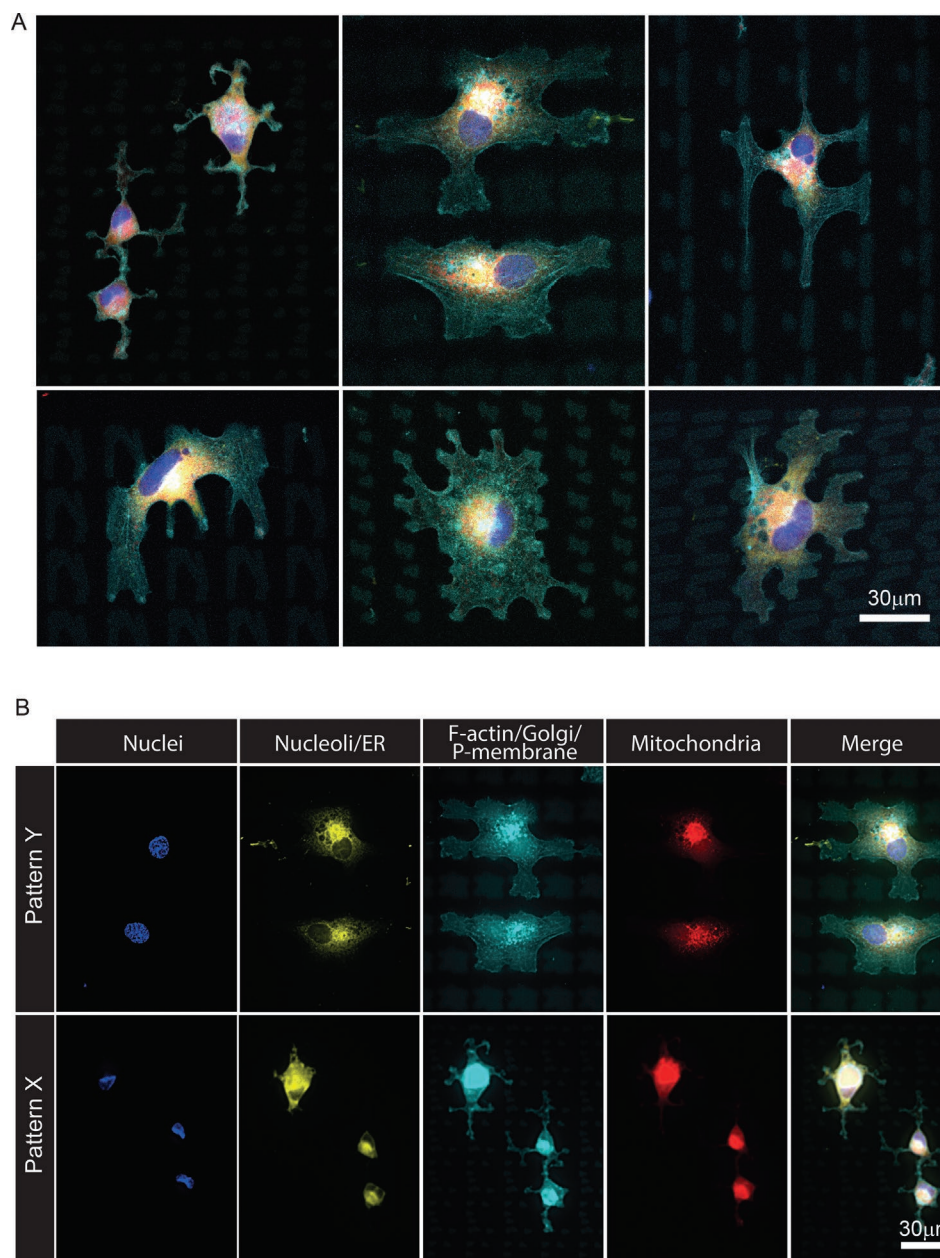
ADVANCED
SCIENCE NEWS
www.advancedsciencenews.com

NANO · MICRO
small
www.small-journal.com

Figure 4. hMSC cell morphology on the Galapagos chip. A) hMSCs cultured for 4 h on the Galapagos chip platform stained with CellPainting assay[70] and shown as merged (nuclei: blue, endoplasmic reticulum (ER) and nucleoli: yellow, F-actin, plasma membrane, and Golgi: cyan, and mitochondria: red). Different cell morphologies are observed on different micropattern units. Scale bar is 30 μm. B) Subcellular organelle morphologies of the cells on the different micropatterns. Cells labeled with CellPainting assay: Hoechst 33342 (nuclei), concanavalin A (ER), SYTO 14 (nucleoli), phalloidin (actin), WGA (Golgi, P-membrane), MitoTracker Deep Red (mitochondria). Scale bar is 30 μm.

and had a mean YAP nuclear-to-cytoplasm ratio of 2.4, which is in the lower part of the distribution curve and is in line with our observations. We observed that different RGD/PEG micropattern units induce different YAP expression levels (i.e., average YAP^{nuc}/YAP^{cyto} fluorescence intensity ratio). In our previous TopoChip work, we noted correlations between topographical design and cell response.[55] To see whether this also applies to YAP staining on the Galapagos chip, we applied a machine-learning algorithm to find a correlation between YAP nuclear translocation and RGD pattern design

parameters (see the Experimental Section for details). In contrast to the relations, we found between topographical design and molecular marker expression,[56,58] no such correlation was found between YAP expression and island design features (Figure S8, Supporting Information). Generally, in the literature, YAP/TAZ is reported to be regulated by cytoskeletal tension caused by cell adhesion, cell spreading, and cell shape on micropatterns.[59,60] On the Galapagos chip, cells can attach to multiple RGD micropatterns, leading to more heterogenous cell spreading and morphological response
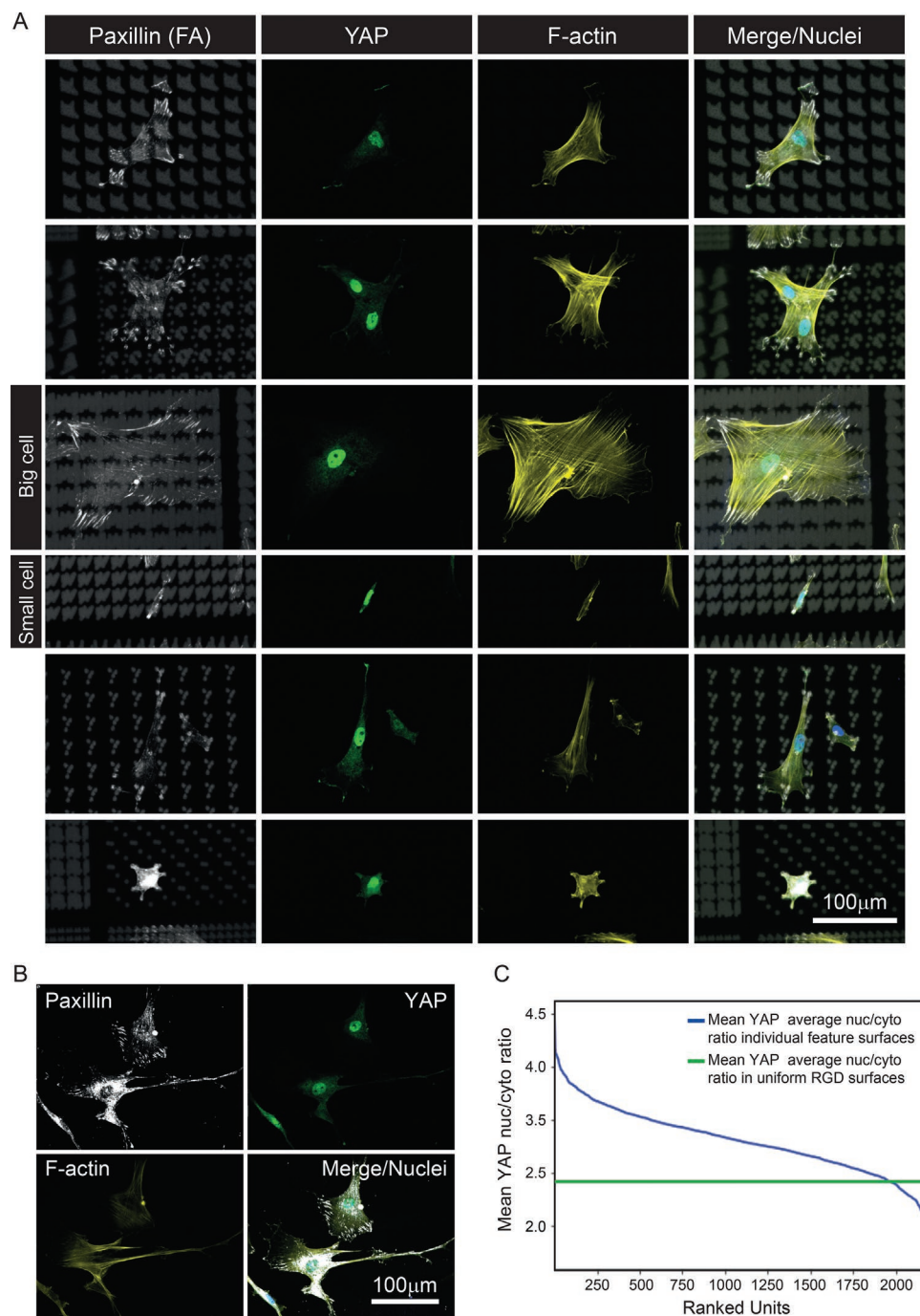
**ADVANCED
SCIENCE NEWS**

www.advancedsciencenews.com

NANO · MICRO

small

www.small-journal.com

Figure 5. Influence of RGD microislands on mechanotransduction in hMSCs. A) Fluorescence microscopy images of hMSCs cultured for 4 h on the Galapagos chip. Cells were stained for paxillin (white), YAP (green), F-actin (yellow), and DNA (blue). Diverse profiles of staining and cell morphologies were observed. One of the smallest and one of the largest cells are shown, as indicated. B) HMSCs cultured on the uniformly grafted RGD surface and stained as indicated. Scale bars are 100 µm. C) Graph representing the mean YAP nuclear translocation levels of hMSCs cultured on the Galapagos chip of each individual microisland unit, ranked from the highest to the lowest. The green line represents the mean YAP translocation level of hMSCs on the nonpatterned uniform RGD surfaces.

within a single micropattern unit than the more homogenous response elicited on the cells by TopoChip topographies (Figure S5, Supporting Information). This may explain the absence of a correlation between YAP and RGD micropattern design.

2.6. YAP Nuclear Localization Correlates with Cell Morphology Features

We recently reported on the correlation between cell shape and gene expression[75] in TopoChip so next, we wanted to know if
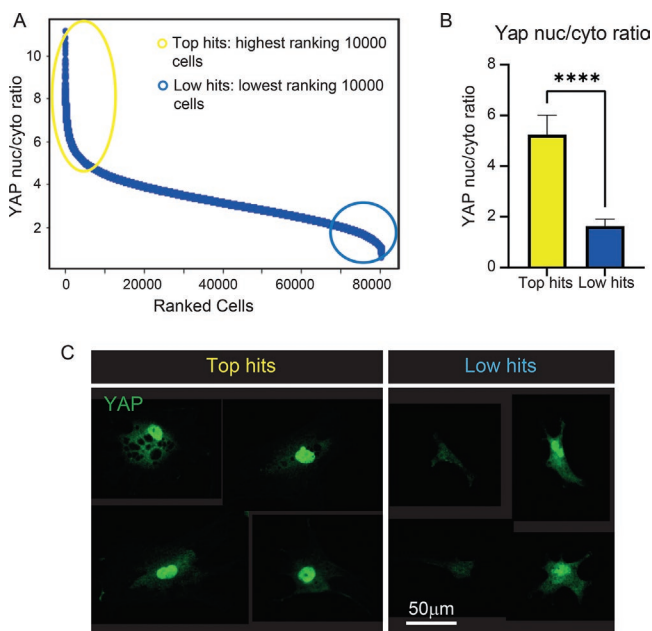
**ADVANCED
SCIENCE NEWS**

www.advancedsciencenews.com

NANO · MICRO

small

www.small-journal.com

Figure 6. YAP expression on the Galapagos chip. A) All cells in the Galapagos chips are ranked according to YAP level from the highest to the lowest. The highest YAP expressing and the lowest YAP expressing 10 000 cells are chosen as the top and low hit cells, as indicated. B) Bar graph representing mean YAP expression levels of either the 10 000 lowest or highest YAP expressing cells (****$p < 0.001$). Error bars represent SD. C) Examples of YAP expressing low- and top-hit cells, which were stained with anti-YAP antibody. Scale bar is 50 µm.

it is possible to use the same screening data to find a correlation between cell morphology and YAP expression. Hereto, we moved from analyzing micropattern unit data (with multiple cells averaged per unit) to single-cell-level data. We extracted 240 cell morphology parameters, such as cell and nucleus solidity, area, and shape, and F-actin and paxillin texture from ≈80 000 cells on the six Galapagos chips using CellProfiler[76] software. First, every cell was ranked for YAP nuclear expression (**Figure 6**A). Remind that Figure 5C presents the mean YAP intensity per unit. To correlate YAP expression to cell morphology parameters, we selected the 10 000 highest- and lowest-ranked cells based on YAP nuclear translocation. The chosen cells are significantly different in YAP nuclear expression (5.6 compared to 1.8, Figure 6B).

We applied the classification algorithm XGBoost to the low- and top-hit cell morphology datasets to find a correlation between nuclear YAP levels and cellular morphology features. We found that the algorithm predicts YAP nuclear translocation based on the cell morphology parameters with an accuracy of 94% and an area under the curve (AUC) of 98% for the training data set, and with an accuracy of 93% and AUC of 97% for the test dataset (**Figure 7**A).

In the model, the cell area and nucleus area were the key features to distinguish low and high YAP together with the nuclear shape parameters eccentricity and solidity, and actin and FA (paxillin) texture parameters (Figure 7C). A scatterplot of cell and nucleus area also showed that high and low YAP cells could be separated based on these features in the test dataset (Figure 7B). In addition, the cell, and nuclear area, the nucleus

eccentricity, the cell, and nuclear perimeter, and paxillin texture feature DifferenceVariance 3_02 (Table S2, Supporting Information) positively correlate with YAP expression, whereas nuclear solidity negatively correlates with YAP expression (Figure 7C). We further confirmed that the YAP high cells have significantly different morphology parameters for the cellular, and nuclear area, paxillin texture-DifferenceVariance 3_02 and actin texture-SumAverage 3_01 than the low-hit YAP level cells (Figure 7D). Visual inspection of YAP high and low cells clearly showed that YAP high cells were much bigger and had bigger nuclei (**Figure 8**). Also, they have thicker and more intense actin stress fibers as well as bigger and longer FAs which is in line with our machine-learning model results as well as with other published results.[60] Our result confirms current literature, in which spreading of hMSCs strongly correlates with nuclear YAP expression.[59,77] However, we found that high YAP did not correlate with cell shape-related morphological parameters, such as cell eccentricity, solidity, etc., which implies that the different cell spreading area, rather than the different cell shape,[78] is related to YAP activation/translocation.

3. Conclusions and Outlook

With this work, we have introduced the Galapagos chip platform as a new and valuable tool to study the effect of cell shape and adhesion on cell physiology in a high-throughput manner. We established Galapagos chip fabrication and a high-throughput screening workflow including cell culture, image processing, and data analysis as outlined in **Figure 9**.

The approach for producing high-quality chemical micropatterns in combination with in silico designed patterns of the TopoChip has a great potential for further development. First, we grafted an integrin ligand (RGD) and antifouling polymer (PEG) to form the Galapagos chip; however, it is possible to employ other integrin ligands,[79,80] cadherin ligands,[68,81] and growth factors[82,83] (full protein or short mimetic peptide). In general, integrin-mediated adhesion and geometric interactions are extensively studied,[34] but there is a huge gap in knowledge about different types of ligand-geometric crosstalk in the literature. Recently, it was reported that spatial distribution of the BMP-2 mimetic peptides can modulate osteogenic differentiation of MSCs without using differentiation medium.[42] In addition, crosstalk between different biochemical ligands such as integrin and growth factors, integrin and cadherin demonstrates synergistic effects on various cell responses and fate. For example, Bilem et al. reported that BMP-2 mimetic peptide and RGD peptide crosstalk has a synergetic effect on MSC osteogenesis,[82,84] and Cosgrove et al. reported HAVDI-RGD (cadherin and integrin ligands) crosstalk on the modulation of MSCs' mechano-sensing.[68] The Galapagos chip system workflow allows the study of the systematic combination and positioning of dual biochemical ligands (Figure 9). Second, the micropattern designs (3–28 µm in size) used in the Galapagos chip can be replaced by any other pattern designs to cover a wider range of scale patterns that could reach 1.656 µm theoretical resolution for our experimental conditions (Figure S3, Supporting Information) using better optics and controlling the thiol solution volume. Third, the described method has enabled
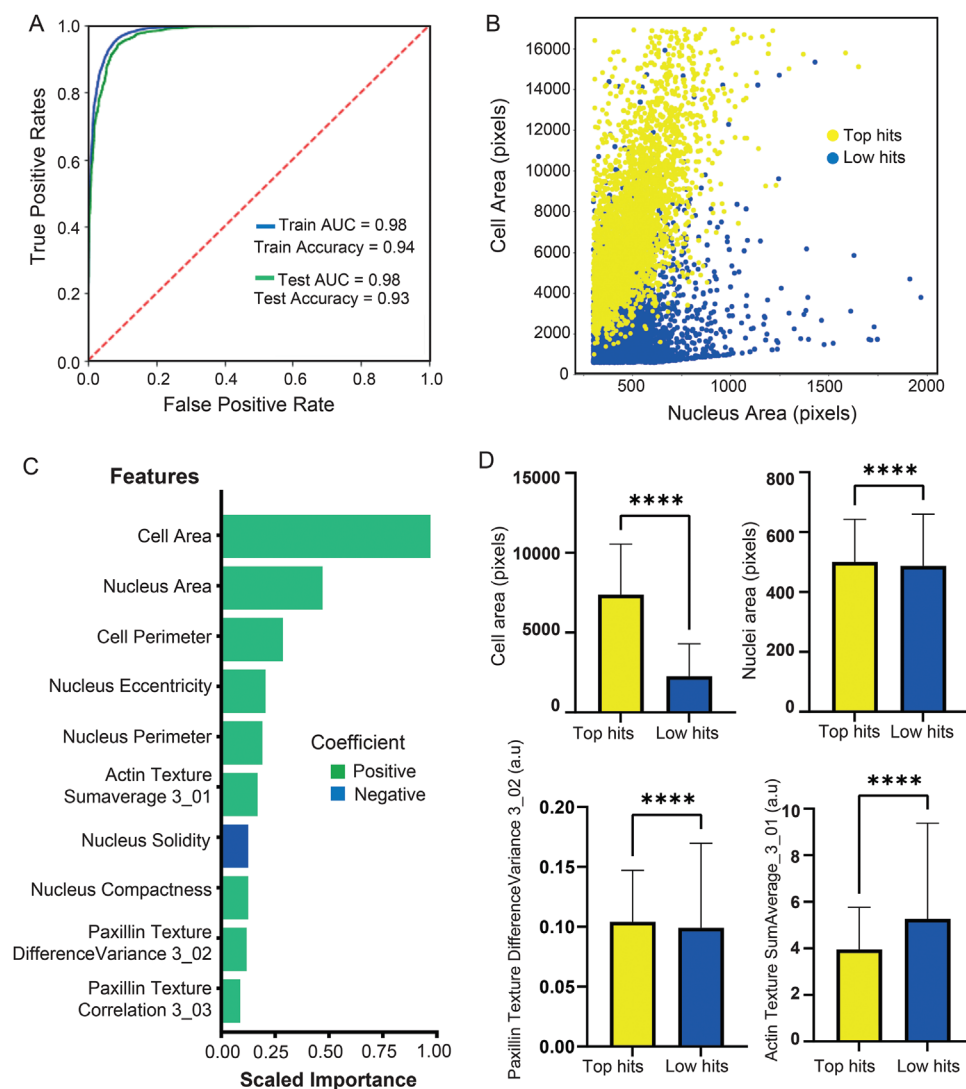
ADVANCED
SCIENCE NEWS
www.advancedsciencenews.com

NANO · MICRO
small
www.small-journal.com

Figure 7. Machine-learning model to predict YAP expression. A) Receiver operating characteristic (ROC) curve showing the prediction performance of YAP expression with the XGBoost classification algorithm for training and test datasets. Area under the curve (AUC) indicates the predictive power of the model. B) Cell area is the most prominent feature, followed by the nuclear area to distinguish low from high YAP expressing MSCs. Scatterplot representing the distribution of the cell and nuclear area for low (blue) and high (yellow) YAP cells in the test dataset. C) Bar diagram representing the importance of cellular morphological parameters/features as predictive factors for YAP expression level through the XGBoost algorithm. The data are scaled by the most important feature: Cell area. Features that influence YAP prediction negatively are shown in blue and a positive influence is shown in green. D) The high YAP expressing cells have significantly different (****$p < 0.001$) morphology parameters for the higher cell and nucleus area, and paxillin texture-DifferenceVariance 3_02 but lower actin texture-SumAverage 3_01 than the low YAP expressing cells. Error bars represent SD.

us to pattern multiple substrates, including inert cell culture polymers, and large areas in a straightforward manner. From a translational tissue engineering and biomaterials designs perspective, we could pattern biomaterial surfaces with selected ligands and any geometry combination from the screening result on the Galapagos chip, using the same grafting strategy and patterning processes consistently for in vivo testing or further applications.

Proof of principle experiments described in this work show the diversity in cellular response and cell morphological/shape change to subcellular chemical patterns. So far, no high-throughput screening platforms have been established in which cell shape is manipulated systematically using adhesive patterns.

Current cell shape/morphology modulation approaches have used simple geometric shapes such as circles, rectangles, and triangles to generate islands for the cells to adhere to and grow on. Alternatively, subcellular adhesive islands have been manufactured for the cells to adhere to, but these islands are typically arranged in regular patterns. In contrast, the Galapagos chip provides cells with an extremely diverse set of adhesive geometries, resulting in a vast array of cell shapes. In addition, from the data we obtained, we built a biologically relevant machine-learning model that predicts YAP nuclear translocation by cell-morphological parameters with 94% accuracy, demonstrating the applicability of micropatterning techniques as a tool to study mechanosensitive signaling in high throughput.
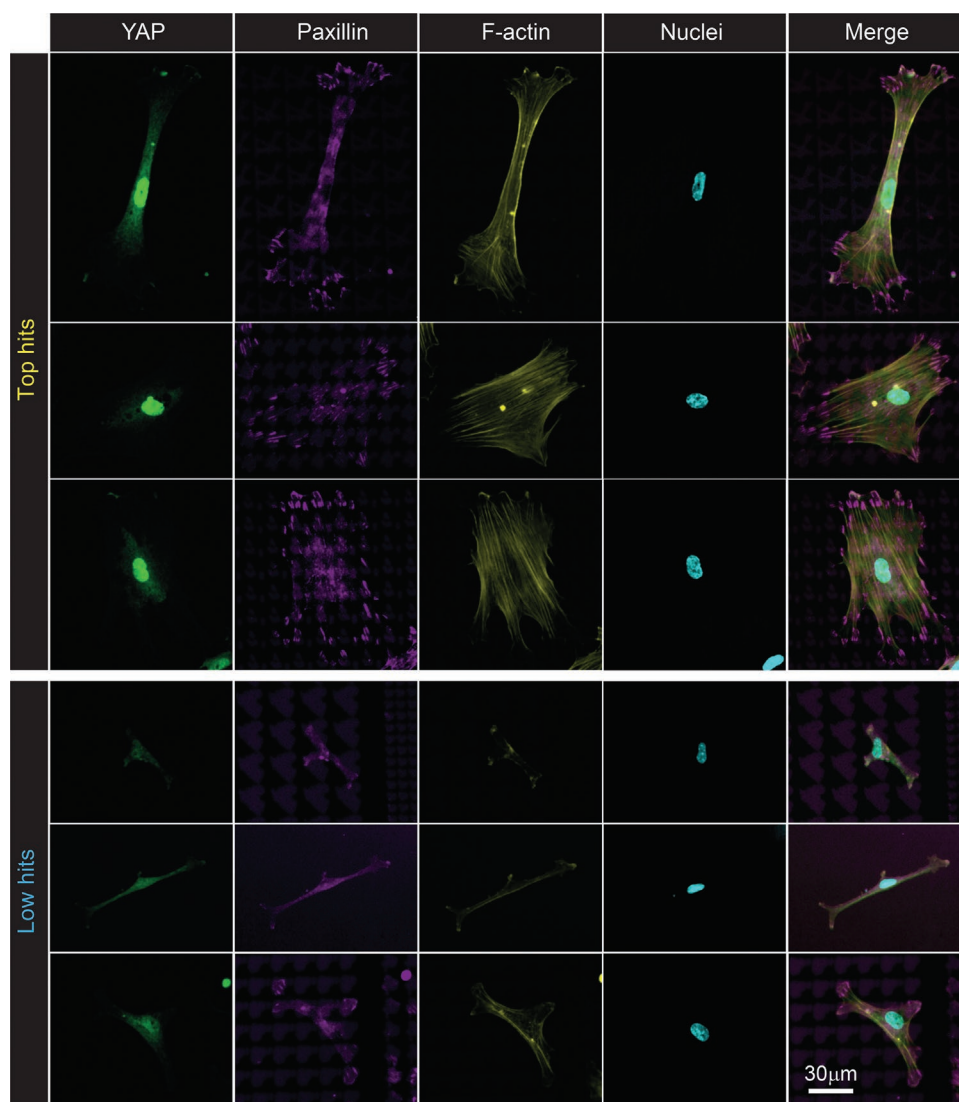
**ADVANCED
SCIENCE NEWS**

www.advancedsciencenews.com

NANO · MICRO

small

www.small-journal.com

Figure 8. Top- and low-hit YAP-expressing cells. hMSCs cultured for 4 h on the Galapagos chip platform stained for YAP (green), paxillin (purple), F-actin (yellow), and nuclei (cyan). On cells with distinct YAP translocation on top and low hits, distinct cell area, nucleus area, paxillin texture, and actin texture are observed. Scale bar is 30 µm.

As most high-throughput screening platform,[54] the Galapagos chip platform is particularly suitable for image-based readouts. It is not suitable for standard biochemical assays because no physical boundaries are present between pattern units, but it can be used for gene expression analysis with laser caption microscopy. Thus, single cells can be identified and isolated from the chip and used for further analysis, e.g., in single-cell RNA sequencing.

In summary, the Galapagos chip platform is a new and valuable tool to study cell–material interaction in a high-throughput manner with a wide variety of applications in the study of mechanobiology and cell–biomaterial interactions.

4. Experimental Section

Materials and Chemicals for Surface Preparations: Hydrogen peroxide (33 wt%), concentrated H_2SO_4, ethanol, and isopropanol were purchased from VWR (Netherlands). Norbornene silane (NbTES) ([bicyclo[2.2.1]hept-5-en-2-yl]triethoxysilane) and lithium phenyl(2,4,6-

trimethyl benzoyl)phosphinate (LAP) photoinitiator were purchased from TCI Chemicals (Netherlands). CGGGRGDS and CGGGRGDSK-FITC peptides were obtained from Chinapeptides (China). Ac-HAVDIGGGC peptide and FITC-PEG (fluorescein-labeled polyethylene glycol thiol, MW = 2 kDa) were purchased from GenScript (USA) and Nanocs (USA), respectively. (Corning) human fibronectin and NHS-rhodamine were obtained from Fisher Scientific (Netherlands). Polymers: PS and PC films were purchased from RS component (Netherlands), and polyethylene (*ibidi* polymer coverslips) (Cat. No: 10813) were purchased from *ibidi* (Germany). All other chemicals were purchased from Sigma-Aldrich (Netherlands) and used as received.

Design of the Mask: The micropatterns were designed by custom-made C++ scripts, according to previous report.[51] Briefly, the primitive shapes, i.e., rectangles, circles, and triangles, 3–10 µm in size, were randomly combined to generate a single feature. The varying feature size, shape, and orientation led to a large pool of unique features. For the platform, 2176 unique features were chosen. Each feature was arrayed in a 290 µm × 290 µm unit to form a single micropattern unit. The platform contained 2176 micropattern units in duplicate in 2 cm × 2 cm. The script created a CleWin (WieWeb software) image file, which was used to create a quartz chromium photomask. The mask was prepared by Delta Mask (The Netherlands).
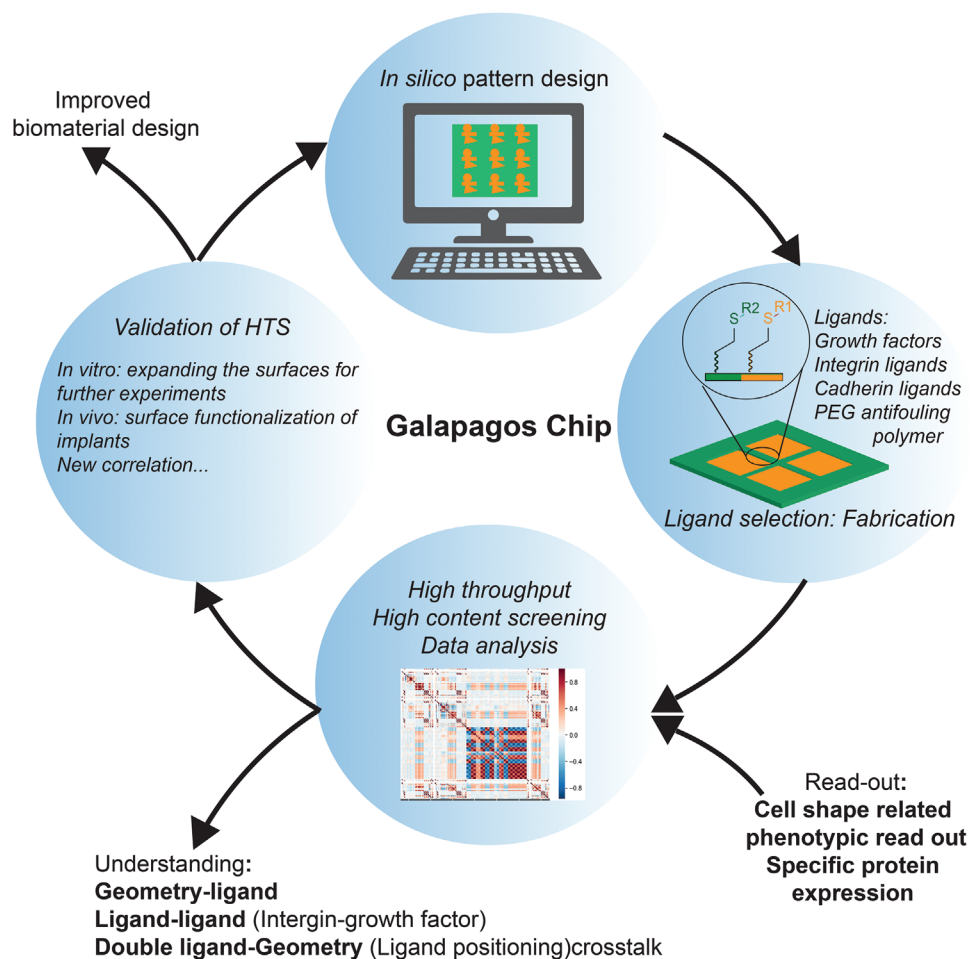
**ADVANCED
SCIENCE NEWS**

www.advancedsciencenews.com

NANO · MICRO

small

www.small-journal.com

Figure 9. Workflow of high-throughput screening with the Galapagos chip. Patterns are designed in silico to prepare a UV mask. The selected binary ligands are transferred via thiol–ene chemistry to produce the Galapagos chip. The geometry–ligand interactions are investigated with high-content imaging and data analysis. This is followed by further investigation of the hit patterns and surfaces or updating the pattern designs.

Surface Functionalization with Silane: *Glass surface activation*: Menzel microscopy glass slides (Boom) were cleaned with ethanol, acetone, and water in an ultrasonication bath for 10 min, respectively. Then, clean slides were immersed in 1 M KOH solution and sonicated for 20 min. Lastly, to generate active hydroxyl groups on the surfaces, piranha cleaning (concentrated H_2SO_4: 30% H_2O_2 = 3:1 v/v) was applied for 30 min. After activation with the piranha solution, the glass slides were washed excessively with distilled water and dried with a nitrogen gun.

Polymer surface activation: The polymer surfaces (polycarbonate, polystyrene, and *ibidi* polymer slides cut into 2.5 cm × 2.5 cm pieces) were cleaned with ethanol, distilled water for 10 min, and 1 M KOH for 20 min. Instead of using a piranha solution, which could etch the polymers, oxygen plasma was used for surface activation of polymers. The plasma treatment was performed for 5 min at 60 W power conditions.

Silanization of the surfaces: For modifying surfaces with alkene silanes, the activated surfaces were placed immediately on a glass petri dish with a 150 μL droplet of silane solution (VTMS or NbTES) and put vacuum oven evacuated at 150–160 mbar pressure and preheated 80 °C for desired period (mostly 24 h). The functionalized surfaces were stored for 4 °C further use.

Thiol–Ene Photocoupling: All the thiol–ene reactions were performed in a CX-2000 Ultraviolet Crosslinker (UVP, 10.0 mW cm^{-2}, 254 nm) with 5 mg mL^{-1} LAP photoinitiator under ambient room conditions except otherwise stated.

Thiol–ene kinetic study: To study thiol–ene reactions, norbornene and vinyl silane functionalized glass slides wetted with a 10×10^{-3} M RGD (CGGGRGDS) peptide water solution and *1H,1H,2H,2H*-perfluorodecanethiol solution in ethanol were irradiated under UV light with the desired period without the addition of a photoinitiator. After the UV exposure, samples were washed with ethanol, and water in an ultrasonication bath for 10 min each and dried with a nitrogen gun.

Uniform surfaces: First, the thiols: RGD (CGGGRGDS) and all polyethylene glycol thiols were dissolved in water, and HAVDI (AcHAVDIGGGC) was dissolved in triethanolamine buffer with 10×10^{-3} M concentration containing 5 mg mL^{-1} LAP photoinitiator. Then, the thiol solution of interest was dropped onto the alkene silane-modified substrate and covered with a fluorinated quartz slide (25 × 60 × 1 mm, from Alfa-Aeser) and irradiated with 254 nm UV light for 10 min. After the UV exposure, samples were washed with ethanol, and water in an ultrasonication bath for 10 min each and dried with a nitrogen gun. Lastly, samples were stored in 70% ethanol for further use.

Binary micropatterned surfaces: To produce the platform with binary micropatterns, a two-step thiol–ene reaction was performed. First, a 10×10^{-3} M RGD peptide solution containing 5 mg mL^{-1} LAP solution was prepared. The 3 μL RGD thiol solution was dropped on the vinyl-modified glass substrate (25 mm × 25 mm × 1 mm), covered by the photomask, and irradiated by UV light for 10 min. The thiol solution volume of the first thiol–ene reaction was critical to transferring the patterns as the gap between the substrate and the mask affected the resolution of the patterns. After removing the photomask,

**ADVANCED
SCIENCE NEWS**

www.advancedsciencenews.com

NANO · MICRO

small

www.small-journal.com

samples were washed with ethanol and water in an ultrasonication bath for 10 min, and dried with a nitrogen gun. The second thiol to graft (10×10^{-3} M PEG thiol or HAVDI peptide solution containing 5 mg mL^{-1} photoinitiator) was dropped onto the patterned surface and covered with fluorinated quartz slide, and irradiated by UV light for another 10 min. Finally, the plate was washed with tetrahydrofuran, ethanol, and water in an ultrasonication bath and dried with a nitrogen gun. The samples were stored in 70% ethanol for further use at 4 °C.

Surface characterizations: A contact angle meter (Drop shape analyzer, DSA25 from KRUSS) was used to measure the static WCA on the different substrates. 4 µL volume water droplets were used with Laplace–Young fitting for contact angle measurements. Fluorescent images of surfaces were taken on a Nikon TE200 inverted fluorescence microscope. The surface chemical compositions were investigated after each step of surface modification by XPS. Measurements were performed using a K-Alpha+ XPS spectrometer (ThermoFisher Scientific, East Grinstead, UK). For data acquisition and processing, the Thermo Avantage software was used. All surfaces were analyzed using a micro-focused, monochromated Al Kα X-ray source (400 µm spot size). The K-Alpha+ charge compensation system was employed during analysis, using electrons of 8 eV energy and low-energy argon ions to prevent any localized charge build-up. The spectra were fitted with one or more Voigt profiles (BE uncertainty: ± 0.2 eV), and Scofield sensitivity factors were applied for quantification.[85] All spectra were referenced to the C 1s peak (C—C, C—H) at 285.0 eV binding energy. Functional groups of the functionalized polymer surfaces were characterized by using an FTIR. The distributions of RGD peptide and PEG mass fragments on the surface were investigated with ToF-SIMS on a TOF.SIMS^5 instrument (ION-TOF GmbH, Münster, Germany). Bi$_3^+$, 25 keV, was used as a primary ion beam with delayed extraction to increase spatial resolution. AFM was performed on AFM (Bruker) in standard tapping mode in the air to measure surface topography.

Cell Culture: MSCs were obtained from a human donor (D201), as previously described.[86] Briefly, isolated hMSCs were expanded in a basic medium, which was consisted of α-minimal essential medium (α-MEM, Life Technologies), supplemented with 10% fetal bovine serum (Sigma Aldrich), 0.2×10^{-3} M ascorbic acid (Life Technologies), 100 U mL^{-1} penicillin (Life Technologies), and 100 mg mL^{-1} streptomycin (Life Technologies). Cells were grown at 37 °C in a humid atmosphere with 5% CO$_2$. The media was changed every 2–3 days. Before cell culture, the substrates were sterilized with 70% ethanol for 20 min and washed three times with phosphate-buffered saline (PBS). Cells were seeded at 8000 cells cm^{-2} at passage five unless stated otherwise.

Immunocytochemistry: The cells were washed with PBS and fixed with 3.7% paraformaldehyde (PFA, Sigma-Aldrich) for 10 min at room temperature. After washing three times, cells were permeabilized with 0.01% Triton X-100 and blocked with 3% bovine serum albumin (BSA) in PBT (PBS + 0.02% Triton-X-100, 0.5% BSA) for 1 h. Afterward, cells were incubated with the primary antibodies dissolved in PBT overnight at 4 °C. Cells were washed three times and incubated with a specific secondary goat antibody conjugated to Alexa Fluor 647 and/or Alexa Fluor 488 (1:400; ThermoFisher), together with phalloidin conjugated to Alexa Fluor 568 (1:250; ThermoFisher) in PBT for 1 h. After washing, the nucleus was counterstained with Hoechst 33258 (1:1000) for 10 min. After washing three times, surfaces were mounted on glass cover slides with a mounting medium (Dako). All washing steps were performed with PBT. Primary antibodies used in this study were: mouse anti-YAP1 antibody (1:200; Santa Cruz, SC-101199) and rabbit anti-paxillin antibody (1:200; Abcam; ab32084). Fixed samples were inverted, and fluorescent images were taken through a glass coverslip using an automated Nikon Eclipse Ti-U microscope with an Andor Zyla 5.5 4MP camera.

CellPainting Assay: The CellPainting assay protocol was adapted from Bray et al.,[70] a variety of subcellular organelles were stained with various fluorescent dyes. Before cell fixation, 500×10^{-9} M of MitoTracker deep red FM (Invitrogen, M22426) was added to the cells for 30 min. Afterward, cells were washed with HBSS (Hank's balanced salt solution, Fisher Scientific, 11540476) and fixed with 4% PFA (VWR, 30525)

for 20 min at room temperature. Samples were permeabilized with 0.1% Triton 100 (VWR, 437002A) for 10 min, followed by washing with HBSS (Fisher Scientific, 11540476). Wheat germ agglutinin Alexa Fluor 594 conjugate (Invitrogen, W11262) at a concentration of 5 µg mL^{-1}, concanavalin A, Alexa Fluor 488 conjugate (Invitrogen, C11252) at a concentration of 50 µg mL^{-1}, SYTO 14 green, fluorescent-nucleic acid stain (Invitrogen, S7576) at a concentration 10×10^{-6} M, 1:40 Alexa Fluor 568 Phalloidin (Thermo Fischer Scientific, A12380) and 1:2000 Hoechst 33342, trihydrochloride, trihydrate (Thermo Fischer, H1399) were further added for 30 min. After washing three times, surfaces were mounted on glass cover slides with a mounting medium (Dako).

Live/Dead Assay: Cell viability was qualitatively assessed for 4 and 24 h of culture with LIVE/DEAD Viability/Cytotoxicity Kit (Thermo Fisher Scientific) assay. Briefly, cells seeded on micropatterned surface and TCP were washed with PBS two times and incubated in 2×10^{-6} M Calcein AM and 6×10^{-6} M ethidium homodimer (EthD-1) in serum-free α-MEM with nucleosides and without phenol red (Thermo Fisher Scientific) for 30 min at 37 °C in the dark, and washed with the medium twice.

Image Analysis: Cell, nucleus shape morphology parameters were extracted with CellProfiler[76] using customized pipelines for cell adhesion and YAP analysis. Each pipeline included background correction, nucleus, and cell segmentations for further cell and nucleus morphology analysis. YAP intensity expression was quantified using the average pixel intensity of the segmented nucleus divided by the average pixel intensity of the segmented cytoplasm of a single cell. In Figure S7 in the Supporting Information, an example of cell segmentation and YAP intensity quantification was shown.

Machine Learning Algorithms for Correlating YAP Expression and Cell Morphology: First, the data were cleaned and combined. To clean the data, thresholds for nucleus area (lower than 300 pixels), YAP nuclear intensity (lower than 0.003), and median intensity ratio YAP^{nuc}/YAP^{cyto} close to 1 (removed $0.95 \leq$ YAP^{nuc}/YAP$^{cyto} \leq 1.05$) were used using the Panda library in Jupyter notebook. Second, to remove inconsistent units, a filter was defined based on the interquartile range of the mean intensity ratio YAP^{nuc}/YAP^{cyto}. For YAP level per pattern and pattern design correlation analysis, the cleaned data were grouped by the feature number (ID; all in the Galapagos chip design had specific ID number), taking the average value of all cells present within that pattern. To identify surface design parameters that influenced the YAP nuclear translocation level, 200 surfaces with the lowest and the highest YAP level were selected for the machine-learning analysis. For YAP-level-to-single-cell-morphology analysis, the 10 000 highest and lowest YAP expressing cells were selected. Before selection, additional filters were used to remove missegmented cells. Cell areas lower than 600 pixels and higher than 18 000 pixels were removed. Prior to data analysis, the features were standardized by removing the mean and scaling-to-unit variance using the StandardScaler function of the "scikit" library. To classify the cells with low- and top-YAP-expressing cells (mean YAP^{nuc}/mean YAP^{cyto}), a classification XGBoost algorithm from the "scikit" library in Python ver. 3.6 was applied. The XGBoost classification algorithm was used to create the predictive models. In order to have a training set for testing the accuracy of the model, the data set was split into two parts randomly by the train_test_split function from the sklearn library in the Jupyter notebook. The first part contained 75% of the data and was used for model training, and the remaining 25% was used for model testing. The classification machine-learning analysis was visualized by the "seaborn" library. The accuracy was depicted by the receiver operating characteristic (ROC) curve, which illustrated the performance of the binary classifier by plotting the true-positive rate against the false-positive rate.

Statistics: All statistical analysis was performed by using GraphPad Prism version 9.0 (GraphPad Software, Inc., San Diego, CA). Student's unpaired *t*-test was carried out for Figures 6 and 7, and Figure S7 in the Supporting Information. One-way analysis of variance was carried out for Figure 2 and Figure S4 in the Supporting Information with Tukey's post hoc test. Significance was set at $p < 0.05$ and indicated by "*" to determine the significance between means. Error bars in figures indicated standard deviation (SD).

Supporting Information

Acknowledgements

Conflict of Interest

The authors declare no conflict of interest.

Data Availability Statement

The data that support the findings of this study are available from the corresponding author upon reasonable request.

Keywords

[1] B. Geiger, J. P. Spatz, A. D. Bershadsky, *Nat. Rev. Mol. Cell Biol.* **2009**, *10*, 21.

[2] A. D. Bershadsky, N. Q. Balaban, B. Geiger, *Annu. Rev. Cell Dev. Biol.* **2003**, *19*, 677.

[3] S. K. Mitra, D. A. Hanson, D. D. Schlaepfer, *Nat. Rev. Mol. Cell Biol.* **2005**, *6*, 56.

[4] N. Borghi, M. Lowndes, V. Maruthamuthu, M. L. Gardel, W. J. Nelson, *Proc. Natl. Acad. Sci. USA* **2010**, *107*, 13324.

[5] Y. J. Liu, M. le Berre, F. Lautenschlaeger, P. Maiuri, A. Callan-Jones, M. Heuzé, T. Takaki, R. Voituriez, M. Piel, *Cell* **2015**, *160*, 659.

[6] B. Trappmann, J. E. Gautrot, J. T. Connelly, D. G. T. Strange, Y. Li, M. L. Oyen, M. A. Cohen Stuart, H. Boehm, B. Li, V. Vogel, J. P. Spatz, F. M. Watt, W. T. S. Huck, *Nat. Mater.* **2012**, *11*, 642.

[7] S. W. Crowder, V. Leonardo, T. Whittaker, P. Papathanasiou, M. M. Stevens, *Cell Stem Cell* **2016**, *18*, 39.

[8] R. McBeath, D. M. Pirone, C. M. Nelson, K. Bhadriraju, C. S. Chen, *Dev. Cell* **2004**, *6*, 483.

[9] K. A. Kilian, B. Bugarija, B. T. Lahn, M. Mrksich, *Proc. Natl. Acad. Sci. USA* **2010**, *107*, 4872.

[10] R. Peng, X. Yao, J. Ding, *Biomaterials* **2011**, *32*, 8048.

[11] C. S. Chen, M. Mrksich, S. Huang, G. M. Whitesides, D. E. Ingber, *Science* **1997**, *276*, 1425.

[12] P. Fiorilli, D. Partridge, I. Staniszewska, J. Y. Wang, M. Grabacka, K. So, C. Marcinkiewicz, K. Reiss, K. Khalili, S. E. Croul, *Lab. Invest.* **2008**, *88*, 1143.

[13] Y. Ikada, *Biomaterials* **1994**, *15*, 725.

[14] C. Holmes, M. Tabrizian, in *Stem Cell Biology and Tissue Engineering in Dental Sciences* (Eds: A. Vishwakarma, P. Sharpe, S. Songtao, M. Ramalingam), Elsevier Inc., New York **2015**, pp. 187–206.

[15] M. M. Stevens, J. H. George, *Science* **2005**, *310*, 1135.

[16] W. Senaratne, L. Andruzzi, C. K. Ober, *Biomacromolecules* **2005**, *6*, 2427.

[17] K. L. Prime, G. M. Whitesides, *J. Am. Chem. Soc.* **1993**, *115*, 10714.

[18] N. Herzer, S. Hoeppener, U. S. Schubert, *Chem. Commun.* **2010**, *46*, 5634.

[19] S. Herrwerth, W. Eck, S. Reinhardt, M. Grunze, *J. Am. Chem. Soc.* **2003**, *125*, 9359.

[20] H. Takahashi, M. Nakayama, M. Yamato, T. Okano, *Biomacromolecules* **2010**, *11*, 1991.

[21] J. O. Zoppe, N. C. Ataman, P. Mocny, J. Wang, J. Moraes, H. A. Klok, *Chem. Rev.* **2017**, *117*, 1105.

[22] K. Y. Tan, M. Ramstedt, B. Colak, W. T. S. Huck, J. E. Gautrot, *Polym. Chem.* **2016**, *7*, 979.

[23] A. Welle, *J. Biomater. Sci., Polym. Ed.* **2004**, *15*, 357.

[24] E. A. Cavalcanti-Adam, T. Volberg, A. Micoulet, H. Kessler, B. Geiger, J. P. Spatz, *Biophys. J.* **2007**, *92*, 2964.

[25] Y. Hao, H. Cui, J. Meng, S. Wang, *J. Photochem. Photobiol., A* **2018**, *355*, 202.

[26] S. Arumugam, S. v Orski, N. E. Mbua, C. Mcnitt, G.-J. Boons, J. Locklin, V. V. Popik, *Pure Appl. Chem.* **2013**, *85*, 1499.

[27] E. A. Roth, T. Xu, M. Das, C. Gregory, J. J. Hickman, T. Boland, *Biomaterials* **2004**, *25*, 3707.

[28] P. Jonkheijm, D. Weinrich, M. Köhn, H. Engelkamp, P. C. M. Christianen, J. Kuhlmann, J. C. Maan, D. Nüsse, H. Schroeder, R. Wacker, R. Breinbauer, C. M. Niemeyer, H. Waldmann, *Angew. Chem., Int. Ed.* **2008**, *47*, 4421.

[29] A. Azioune, M. Storch, M. Bornens, M. Théry, M. Piel, *Lab Chip* **2009**, *9*, 1640.

[30] B. Colak, S. di Cio, J. E. Gautrot, *Biomacromolecules* **2018**, *19*, 1445.

[31] X. Yao, R. Peng, J. Ding, *Adv. Mater.* **2013**, *25*, 5257.

[32] Y. Shao, J. Fu, *Adv. Mater.* **2014**, *26*, 1494.

[33] Y. Li, Y. Xiao, C. Liu, *Chem. Rev.* **2017**, *117*, 4376.

[34] M. Théry, *J. Cell Sci.* **2010**, *123*, 4201.

[35] M. D. Cabezas, B. Meckes, C. A. Mirkin, M. Mrksich, *ACS Nano* **2019**, *13*, 11144.

[36] M. Arnold, E. A. Cavalcanti-Adam, R. Glass, J. Blümmel, W. Eck, M. Kantlehner, H. Kessler, J. P. Spatz, *ChemPhysChem* **2004**, *5*, 383.

[37] R. Oria, T. Wiegand, J. Escribano, A. Elosegui-Artola, J. J. Uriarte, C. Moreno-Pulido, I. Platzman, P. Delcanale, L. Albertazzi, D. Navajas, X. Trepat, J. M. García-Aznar, E. A. Cavalcanti-Adam, P. Roca-Cusachs, *Nature* **2017**, *552*, 219.

[38] P. Han, J. E. Frith, G. A. Gomez, A. S. Yap, G. M. O'Neill, J. J. Cooper-White, *ACS Nano* **2019**, *13*, 11129.

[39] T. C. von Erlach, S. Bertazzo, M. A. Wozniak, C. M. Horejs, S. A. Maynard, S. Attwood, B. K. Robinson, H. Autefage, C. Kallepitis, A. del Río Hernández, C. S. Chen, S. Goldoni, M. M. Stevens, *Nat. Mater.* **2018**, *17*, 237.

[40] J. T. Connelly, J. E. Gautrot, B. Trappmann, D. W. M. Tan, G. Donati, W. T. S. Huck, F. M. Watt, *Nat. Cell Biol.* **2010**, *12*, 711.

[41] F. M. Watt, P. W. Jordan, C. H. O'Neill, *Proc. Natl. Acad. Sci. USA* **1988**, *85*, 5576.

[42] I. Bilem, L. Plawinski, P. Chevallier, C. Ayela, E. D. Sone, G. Laroche, M. C. Durrieu, *J. Biomed. Mater. Res., Part A* **2018**, *106*, 959.

[43] J. Seo, J. Y. Shin, J. Leijten, O. Jeon, G. Camci-Unal, A. D. Dikina, K. Brinegar, A. M. Ghaemmaghami, E. Alsberg, A. Khademhosseini, *Biomaterials* **2018**, *153*, 85.

[44] M. B. Oliveira, J. F. Mano, *Trends Biotechnol.* **2014**, *32*, 627.

[45] R. Lei, S. Kumar, *Curr. Opin. Solid State Mater. Sci.* **2020**, *24*, 100871.

[46] N. Groen, M. Guvendiren, H. Rabitz, W. J. Welsh, J. Kohn, J. de Boer, *Acta Biomater.* **2016**, *34*, 133.

[47] A. D. Rape, M. Zibinsky, N. Murthy, S. Kumar, *Nat. Commun.* **2015**, *6*, 8129.

[48] Y. Mei, C. Cannizzaro, H. Park, Q. Xu, S. R. Bogatyrev, K. Yi, N. Goldman, R. Langer, D. G. Anderson, *Small* **2008**, *4*, 1600.

[49] Y. Mei, K. Saha, S. R. Bogatyrev, J. Yang, A. L. Hook, Z. I. Kalcioglu, S. W. Cho, M. Mitalipova, N. Pyzocha, F. Rojas, K. J. van Vliet, M. C. Davies, M. R. Alexander, R. Langer, R. Jaenisch, D. G. Anderson, *Nat. Mater.* **2010**, *9*, 768.

[50] Y. Y. I. Amin, K. Runager, F. Simoes, A. Celiz, V. Taresco, R. Rossi, J. J. Enghild, L. A. Abildtrup, D. C. E. Kraft, D. S. Sutherland, M. R. Alexander, M. Foss, R. Ogaki, *Adv. Mater.* **2016**, *28*, 1472.

[51] H. v. Unadkat, M. Hulsman, K. Cornelissen, B. J. Papenburg, R. K. Truckenmüller, G. F. Post, M. Uetz, M. J. T. Reinders, D. Stamatialis, C. A. van Blitterswijk, J. de Boer, *Proc. Natl. Acad. Sci. USA* **2011**, *108*, 16565.

[52] F. F. B. Hulshof, Y. Zhao, A. Vasilevich, N. R. M. Beijer, M. de Boer, B. J. Papenburg, C. van Blitterswijk, D. Stamatialis, J. de Boer, *Acta Biomater.* **2017**, *62*, 188.

[53] J. Hu, A. A. Gondarenko, A. P. Dang, K. T. Bashour, R. S. O'Connor, S. Lee, A. Liapis, S. Ghassemi, M. C. Milone, M. P. Sheetz, M. L. Dustin, L. C. Kam, J. C. Hone, *Nano Lett.* **2016**, *16*, 2198.

[54] N. R. M. Beijer, A. S. Vasilevich, B. Pilavci, R. K. Truckenmüller, Y. Zhao, S. Singh, B. J. Papenburg, J. de Boer, *Adv. Biosyst.* **2017**, *1*, 1700002.

[55] F. F. B. Hulshof, B. Papenburg, A. Vasilevich, M. Hulsman, Y. Zhao, M. Levers, N. Fekete, M. de Boer, H. Yuan, S. Singh, N. Beijer, M. A. Bray, D. J. Logan, M. Reinders, A. E. Carpenter, C. van Blitterswijk, D. Stamatialis, J. de Boer, *Biomaterials* **2017**, *137*, 49.

[56] A. Reimer, A. Vasilevich, F. Hulshof, P. Viswanathan, C. A. van Blitterswijk, J. de Boer, F. M. Watt, *Sci. Rep.* **2016**, *6*, 18948.

[57] M. J. Vassey, G. P. Figueredo, D. J. Scurr, A. S. Vasilevich, S. Vermeulen, A. Carlier, J. Luckett, N. R. M. Beijer, P. Williams, D. A. Winkler, J. de Boer, A. M. Ghaemmaghami, M. R. Alexander, *Adv. Sci.* **2020**, *7*, 1903392.

[58] S. Vermeulen, A. Vasilevich, D. Tsiapalis, N. Roumans, P. Vroemen, N. R. M. Beijer, A. Dede Eren, D. Zeugolis, J. de Boer, *Acta Biomater.* **2019**, *83*, 277.

[59] G. Nardone, J. Oliver-De La Cruz, J. Vrbsky, C. Martini, J. Pribyl, P. Skládal, M. Pešl, G. Caluori, S. Pagliari, F. Martino, Z. Maceckova, M. Hajduch, A. Sanz-Garcia, N. M. Pugno, G. B. Stokin, G. Forte, *Nat. Commun.* **2017**, *8*, 15321.

[60] S. Dupont, L. Morsut, M. Aragona, E. Enzo, S. Giulitti, M. Cordenonsi, F. Zanconato, J. le Digabel, M. Forcato, S. Bicciato, N. Elvassore, S. Piccolo, *Nature* **2011**, *474*, 179.

[61] S. Somasundaram, *J. Biomed. Mater. Res., Part B* **2018**, *106*, 2901.

[62] M. J. Kade, D. J. Burke, C. J. Hawker, *J. Polym. Sci., Part A: Polym. Chem.* **2010**, *48*, 743.

[63] A. B. Lowe, *Polym. Chem.* **2014**, *5*, 4820.

[64] W. Yoshida, R. P. Castro, J. D. Jou, Y. Cohen, *Langmuir* **2001**, *17*, 5882.

[65] C. K. Dixit, S. K. Vashist, B. D. MacCraith, R. O'Kennedy, *Nat. Protoc.* **2011**, *6*, 439.

[66] J.-J. Chen, K. N. Struk, A. B. Brennan, *Langmuir* **2011**, *27*, 13754.

[67] U. Hersel, C. Dahmen, H. Kessler, *Biomaterials* **2003**, *24*, 4385.

[68] B. D. Cosgrove, K. L. Mui, T. P. Driscoll, S. R. Caliari, K. D. Mehta, R. K. Assoian, J. A. Burdick, R. L. Mauck, *Nat. Mater.* **2016**, *15*, 1297.

[69] M. Sun, J. Deng, Z. Tang, J. Wu, D. Li, H. Chen, C. Gao, *Colloids Surf., B* **2014**, *122*, 134.

[70] M. A. Bray, S. Singh, H. Han, C. T. Davis, B. Borgeson, C. Hartland, M. Kost-Alimova, S. M. Gustafsdottir, C. C. Gibson, A. E. Carpenter, *Nat. Protoc.* **2016**, *11*, 1757.

[71] D. Lehnert, B. Wehrle-Haller, C. David, U. Weiland, C. Ballestrem, B. A. Imhof, M. Bastmeyer, *J. Cell Sci.* **2004**, *117*, 41.

[72] A. Mammoto, T. Mammoto, D. E. Ingber, *J. Cell Sci.* **2012**, *125*, 3061.

[73] N. Wang, J. D. Tytell, D. E. Ingber, *Nat. Rev. Mol. Cell Biol.* **2009**, *10*, 75.

[74] M. Théry, A. Pépin, E. Dressaire, Y. Chen, M. Bornens, *Cell Motil. Cytoskeleton* **2006**, *63*, 341.

[75] A. S. Vasilevich, S. Vermeulen, M. Kamphuis, N. Roumans, S. Eroumé, D. G. A. J. Hebels, J. van de Peppel, R. Reihs, N. R. M. Beijer, A. Carlier, A. E. Carpenter, S. Singh, J. de Boer, *Sci. Rep.* **2020**, *10*, 18988.

[76] A. E. Carpenter, T. R. Jones, M. R. Lamprecht, C. Clarke, I. H. Kang, O. Friman, D. A. Guertin, J. H. Chang, R. A. Lindquist, J. Moffat, P. Golland, D. M. Sabatini, *Genome Biol.* **2006**, *7*, R100.

[77] J. E. Sero, C. Bakal, *Cell Syst.* **2017**, *4*, 84.

[78] F. A. Gegenfurtner, B. Jahn, H. Wagner, C. Ziegenhain, W. Enard, L. Geistlinger, J. O. Rädler, A. M. Vollmar, S. Zahler, *J. Cell Sci.* **2018**, *131*, jcs212886.

[79] J. Zhao, F. Santino, D. Giacomini, L. Gentilucci, *Biomedicines* **2020**, *8*, 307.

[80] T. A. Petrie, J. E. Raynor, C. D. Reyes, K. L. Burns, D. M. Collard, A. J. García, *Biomaterials* **2008**, *29*, 2849.

[81] L. Gao, R. McBeath, C. S. Chen, *Stem Cells* **2010**, *28*, 564.

[82] I. Bilem, P. Chevallier, L. Plawinski, E. D. Sone, M. C. Durrieu, G. Laroche, *Acta Biomater.* **2016**, *36*, 132.

[83] B. P. Eliceiri, *Circ. Res.* **2001**, *89*, 1104.

[84] I. Bilem, P. Chevallier, L. Plawinski, E. D. Sone, M. C. Durrieu, G. Laroche, *ACS Biomater. Sci. Eng.* **2017**, *3*, 2514.

[85] J. H. Scofield, *J. Electron Spectrosc. Relat. Phenom.* **1976**, *8*, 129.

[86] A. Mentink, M. Hulsman, N. Groen, R. Licht, K. J. Dechering, J. van der Stok, H. A. Alves, W. J. Dhert, E. P. van Someren, M. J. T. Reinders, C. A. van Blitterswijk, J. de Boer, *Biomaterials* **2013**, *34*, 4592.